Chapter

# X-Rays and Computed Tomography Scan Imaging: Instrumentation and Medical Applications

*Reda R. Gharieb*

## Abstract

This chapter gives a review for both conventional $X$-ray and computed tomography (CT) scan imaging modalities and their medical applications. The chapter presents a brief history on the discovery of $X$-ray, $X$-ray imaging, and computed tomography scan. The linear projection for the generation of the sinogram (the detector's signals versus the rotational angle) and the filtered backprojection for image reconstruction are discussed. Computer simulations for linear and fan beams $X$ -ray are also presented. The chapter discusses some medical applications of both the conventional $X$-ray and CT scan imaging.

**Keywords:** X-ray tube, X-ray, bremsstrahlung, photons and electromagnetic waves, X-ray and dual x-ray imaging, CT scan imaging, linear projection, filtered backprojection, medical applications, chest, abdomen, bones, Covid-19

## 1. Introduction

In 1895, German physicist Wilhelm C. Roentgen accidentally noticed that a cathode-ray tube could make a sheet of paper coated with barium platinocyanide glow [1, 2]. This effect was even while the tube and the paper were in separate rooms. Roentgen decided that the tube must be emitting some sort of penetrating rays, which he named them $X$ for unknown. Shortly afterward, Roentgen aimed the $X$-rays through Mrs. Roentgen's hand at a chemically coated screen. He could see the bones in the hand clearly on the screen. In 1905, Robert Kienböck, a German radiologist, could identify what named Kienböck's disease, using strips of silver bromide photographic paper to estimate the amount of radiation to which patients were exposed in radiation therapy [3–6]. Then, over the next few decades, $X$-rays grew into a widely used diagnostic tool. The image used to be captured on an $X$-ray-sensitive film. Technology advances of electronics made use of $X$-ray for digital imaging by replacing the traditional $X$-ray-sensitive film by electronic sensors [7–10]. Today, both convention and digital $X$-ray imaging modalities are the prompt and main diagnostic tools for investigating and screening the chest for viral and bacterial pneumonia, tuberculosis, lung cancer [11–19], enlarged heart, and blocked blood vessels [20–24]; the bones and teeth for fractures and infections, arthritis, bone cancer, and dental decay [25–30]; the abdomen for digestive tract problems and looking for swallowed items [31]. Moreover, other modalities for $X$-ray imaging have been developed such as digital mammography for breast cancer screening [32]. It is a special imaging technique that employs $X$-ray with low dose of energy. Dual-energy X-ray has also been developed and used for measuring bone mineral density (BMD) [33, 34]. In this technique, two different X-ray beams with different energy values are used.

The history of computed tomography (CT) scan has been around for almost 50 years. It was created by British engineer Godfrey Hounsfield of EMI Laboratories in 1972 [35], **Figure 1**. He co-invented the technology with physicist Dr. Allan Cormack. CT uses a computer algorithm to reconstruct an image from the intensity projections collected by detectors for all angles of rotation of both X-ray source and the detectors around the target; such an image is called a slice. Next slice is obtained after moving the target a step inside the gantry and repeating the rotation, collection, and reconstruct. This made it possible to detect diseases at the earliest stages. At the same time, the radiation load is minimal. Important advantages of CT scan are as follows: the possibility of obtaining three-dimensional images of internal organs, the speed of the performing, comfort of the patient. CT scan has been used for investigating and screening many organs and for different diseases [36–48]. Moreover, it could be used for brain imaging. For a CT scan slice, detectors acquire data versus rational angles, and the slice image is reconstructed by backprojection and filtered backprojection algorithms [49–55]. This chapter highlights instrumentation aspects and medical applications of conventional and CT scan X-ray technology.

## 2. $X$-ray and CT scan instruments

### 2.1 $X$-ray tube and generation of $X$-ray

$X$-ray tube consists of four main parts: the tube, the high-voltage generator, the control console, and the cooling system. The tube has a cathode filament heated by a small voltage providing a small current of few amps. When the filament is heated up, the electrons in the conduction wire start breaking free. To accelerate these electrons toward the anode, a strong electrical potential $(30 - 150)KV$ is maintained between the anode and the cathode. Electrons that break free of the cathode are

**Figure 1.**
*Sir Godfrey Hounsfield with the first commercial CT scanner: http://www.edubilla.com/inventor/godfrey-hounsfield/.*

strongly attracted to the anode disc. The electron flow between the cathode and the anode accounts for the tube current and is in the range of milliamps ($mA$). This current is controlled by regulating the filament current generated by the heating low voltage applied to the cathode circuit. The higher the temperature of the filament, the larger the number of electrons that leave the cathode and travel toward the anode. By controlling the filament temperature, the control console regulates the value of the filament current and hence the intensity of the $X$-ray output. **Figure 2** shows an illustrative $X$-ray tube, which consists of a vacuum glass with the node on one side and the cathode on the other side. The cathode, which is a filament being heated up, is the source of electrons. These electrons are accelerated by the applied high potential between the anode (positive terminal) and the cathode (negative terminal). The accelerated electrons, the electrons with high kinetic energy, bombarding the anode, penetrate the heavy-metal target, for example, tungsten, attached to the anode. Some of these electrons travel close to the nucleus of the heavy metal under the attraction force of its positive charge and are subsequently influenced by its electric field. Thus, these electrons would be deflected, and a portion or all of their kinetic energy would be lost. The principle of the conservation of energy states that in producing the $X$-ray photon, the electron has lost some of its kinetic energy (KE), which should be the energy of the $X$-ray photon. That is,

$$Final\ KE\ of\ electron = Initial\ KE\ of\ electron - Energy\ of\ X\_ray\ photon \tag{1}$$

Thus, $X$-ray is an electromagnetic radiation (photons) of extremely short wavelength with wavelengths ranging from about $10^{-8}$ to $10^{-12}$*meter* and corresponding very high frequencies from about $10^{16}$ to $10^{20}$ Hertz (Hz).

The energy of each photon is determined according to the plank's equation:

$$Energy\ of\ X\_ray\ photon = hf = \frac{hc}{\lambda} \tag{2}$$

where $h = 4.14 \times 10^{-15} eVs$ is the Plank's constant, and $c = 3 \times 10^{8} m/sec$ is the speed of light and $\lambda$ is the wavelength in *meter*. **Figure 3** shows the Bremsstrahlung spectrum of tungsten X-ray. It is obvious that the maxim number of photons occurs at energy of 60 Kev. The photons of low energy are removed from the ray using filtering technique. Such filtering reduces the dose of low-energy photons exposing the patient.

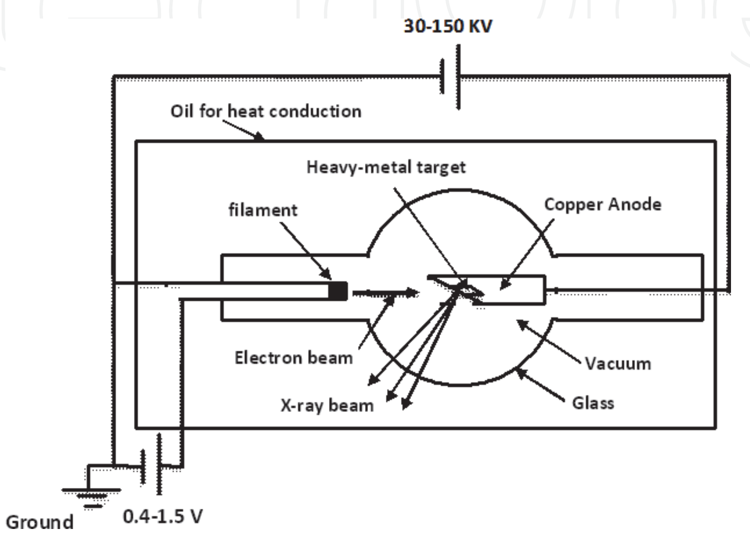


**Figure 2.**
*X-ray tube.*

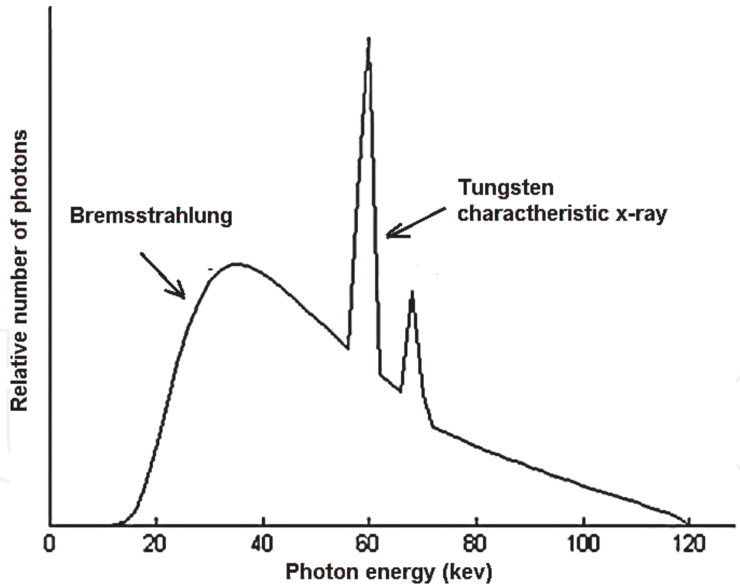


**Figure 3.**
*Bremsstrahlung (brake spectrum) of tungsten.*

1. *X*-ray imaging of human body

2. Non-digital imaging

When a human body is exposure to *X*-rays, the body soft tissue, such as the skin and organs, cannot absorb the high-energy rays, and the beam passes through them. However, dense tissues inside the human's bodies, such as bones, absorb the radiation. The amount of radiation passing through the tissue is detected on the other side by an *X*-ray-sensitive film for non-digital imaging. The film is made of gelatin-covered polyester base or cellulose base coated on one side or two sides by radio-sensitive emulsion, and the emulsion consists of silver halide crystals immersed in gelatin. The emulsion layer is sensitive to *X*-ray. After the exposure of the film to *X*-rays, it is processed to convert the latent image into visible one [56]. The film after being processed provides a grayscale image from black to white. The whiter a region of an *X*-ray image, the lesser the exposure of this region to *X*-ray and hence the denser the tissue corresponding to this image region. Bones and air show themselves, in an *X*-ray image, as white and black, respectively.

## 2.2 Digital *X*-ray imaging

In digital X-ray imaging, instead of using an *X*-ray-sensitive film to capture an image, a planar array of electronic sensors/detectors is used to capture the *X*-ray image [55]. Each electrical detector generates a signal, where its intensity is proportional to the number photons reached this detector. The output of the planar arrays can be displayed on a computer monitor as a grayscale image. These digital images can be stored on a hard drive and can be exchanged on the Internet between different clinical centers. There are two digital detection techniques, the first is called direct technique and the second is called indirect one:

### *2.2.1 Direct technique*

Amorphous silicon (a-Si) or amorphous selenium (a-Se) is used to generate positive charges proportional to X-ray intensity [10, 55–57]. These positive charges

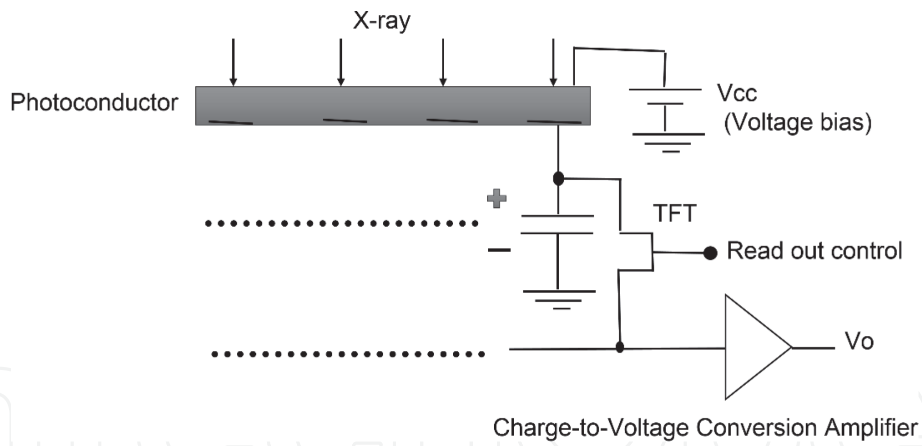


**Figure 4.**
*Direct digital X-ray image capture. One pixel in a cross section of a linear array, all pixels in the array are similar. The readout control selects the pixel being readout. In a planar array, two readout controls are used for selecting the row and the column of the readout pixel. Advances in semiconductor electronics made it possible to fabricate a matrix of such single detector [10, 57].*

are stored in capacitors until they are readout. The capacitor charge corresponding to each pixel is read using a thin flat transistor (TFT) and is converted to voltage, using a charge-to-voltage amplifier. **Figure 4** shows a single detector for one pixel. A matrix consisting of many single detectors can be fabricated similar to the one used in CCD (charge-coupled display).

### *2.2.2 Indirect technique*

In this technique, the *X*-ray is first converted into visible light using an *X*-ray scintillator. Common materials used as scintillator are the gadolinium oxysulfide (GdO2S2) and cesium iodide (CsI) [10, 55–57]. A planar array of photodiodes, TFTs, and capacitors equal to the image size in pixels are used to detect the visible light. Each photodiode generates a current proportional to the intensity of light reached it, and this current is stored as a charge in the capacitor. The capacitor charge is read out using TFT and converted to voltage, using a charge-to-voltage conversion amplifier. **Figure 5** shows a detector element for one pixel.

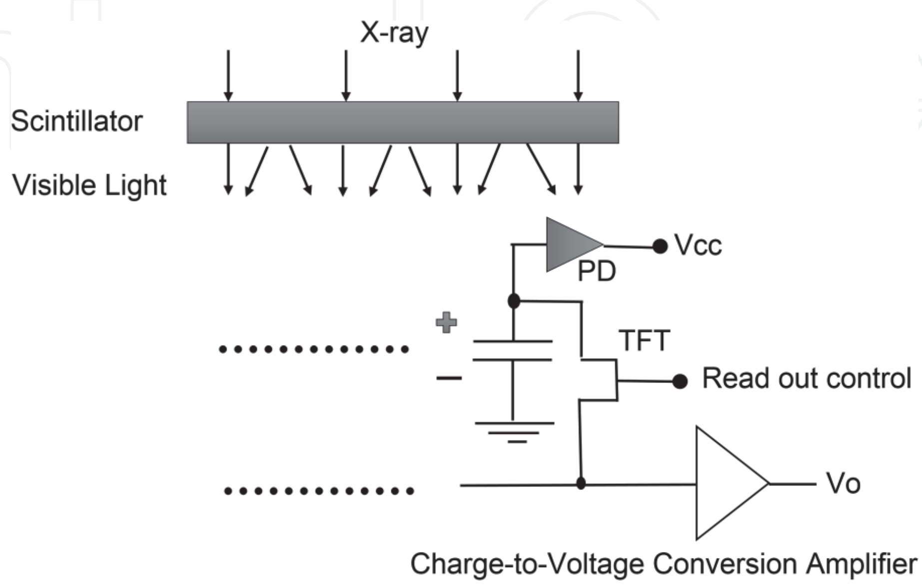


**Figure 5.**
*Indirect digital X-ray image capture. One pixel in a cross section of a linear array, all pixels in the array or matrix are similar. The readout control signal selects the column and row of the pixel being readout.*

## 3. CT scan imaging

### 3.1 CT scan machine

In conventional $X$-ray machine, one image of the body tissue is recorded by sending one beam of $X$-ray through the body from one side and detected attenuated $X$-ray beam from the body's other side. However, in CT scan machine, the patient lies on a table that moves through a doughnut-like ring known as a gantry. In each longitudinal position of the patient's table, a series of $X$-ray data are collected from different angles around the body. This is by enabling the $X$-ray tube and the $X$-ray detector array to rotate around the body. A computer algorithm is sued to generate an axial image called a slice from all $X$-ray data collected from all angles around the body position. Next slice is obtained by moving the patient's table through the gantry and repeating the rotation of $X$-ray tube and the detector array and collecting the $X$-ray data from all angles around the patient at this new position. **Figure 6** shows an illustrative sectional diagram for a CT scan machine.

### 3.2 Computed tomography (CT)

Computed tomography consists of two main steps. The first one is the acquisition of $X$-ray passing tissue, by different detectors from different angles around the target. This is carried out by shining $X$-ray beam on the target and detecting the amount of passed $X$-rays reached at each detector on the opposite side. This acquired data is mathematically explained by the theory of linear projection. The acquiring step provides the sinogram, which is the $X$-ray intensity at each detector versus rotational angles around the body. The second step is the reconstruction of the image from the acquired sinogram. This image reconstruction, the reverse process, is explained by the theory of backprojection.

#### *3.2.1 Linear beam projection*

In **Figure 7**, an $X$-ray passes through a target from the source to the detector on the line determined by the parameters: the distance, $-\infty \le s \le \infty$, in cm and the angle, $0 \le \theta \le \pi$, in degree. The intensity of this $X$ -ray, at the detector, is given by

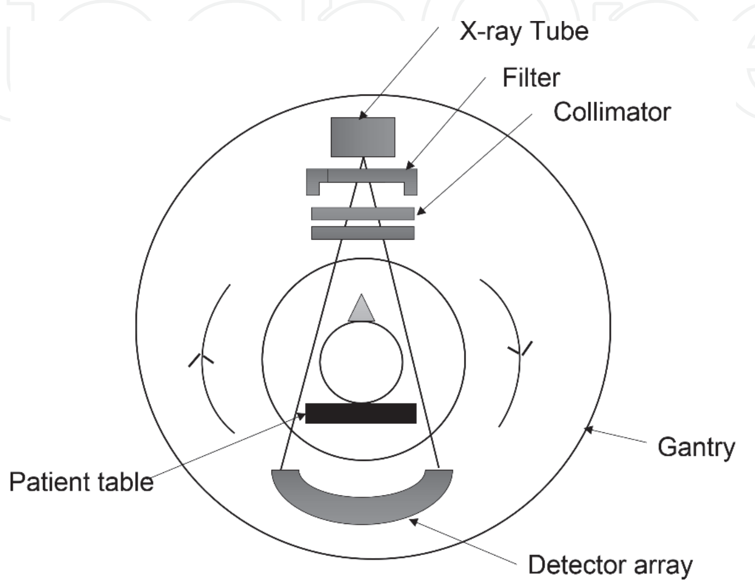


**Figure 6.**
*An illustrative sectional diagram of a CT scan machine.*

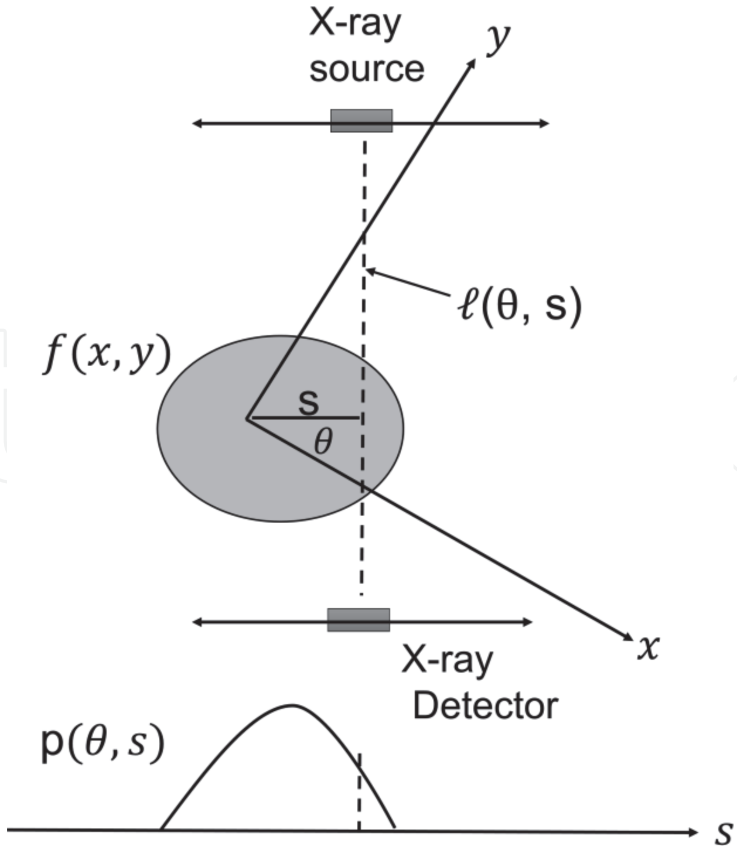


**Figure 7.**
*An intensity function $f(x,y)$ and the linear projection $p(\theta,s)$ versus the distance $s$ at certain angle $0 \le \theta \le \pi$.*

$$I = I_0 e^{-\int_{\ell(\theta,s)} f(x,y)dxdy} \tag{3}$$

where $I_0$ is the intensity at the source. Simply to get the projection $\int_{\ell(\theta,s)} f(x,y)dxdy$, the logarithmic can be used

$$p(\theta,s) = ln\left(\frac{I_0}{I}\right) = \int_{\ell(\theta,s)} f(x,y)dxdy \tag{4}$$

Notice that this logarithmic operation is implemented naturally by different detectors. Thus, the detected value $ln\left(\frac{I_0}{I}\right)$ or the projection $p(\theta,s)$ is a linear integration of absorption coefficients of all voxels over the line $\ell(\theta,s)$. This line is parameterized by $\theta$ and $s$ as follows

$$\ell(\mathrm{\theta, s}) = \{(\mathrm{x, y}) : \mathrm{xcos(\theta) + ysin(\theta) = s}\} \tag{5}$$

Also Eq. (4) can be written as

$$p(\theta,s) = \int_x \int_y f((x,y)\delta(xcos(\theta) + y\ \sin(\theta) - s)dxdy \tag{6}$$

where $\delta(0) = 1$.

It is obvious that due to the integration of the absorption coefficients of all voxels on the line $\ell(\theta,s)$, we lost the information about which voxels on the line have high or low absorption coefficients. **Figure 8(a)** shows a computer simulation scenario in which an intensity function has three objects with different absorption coefficients and sizes. We use 513 samples on $s$ uniformly distributed, which means

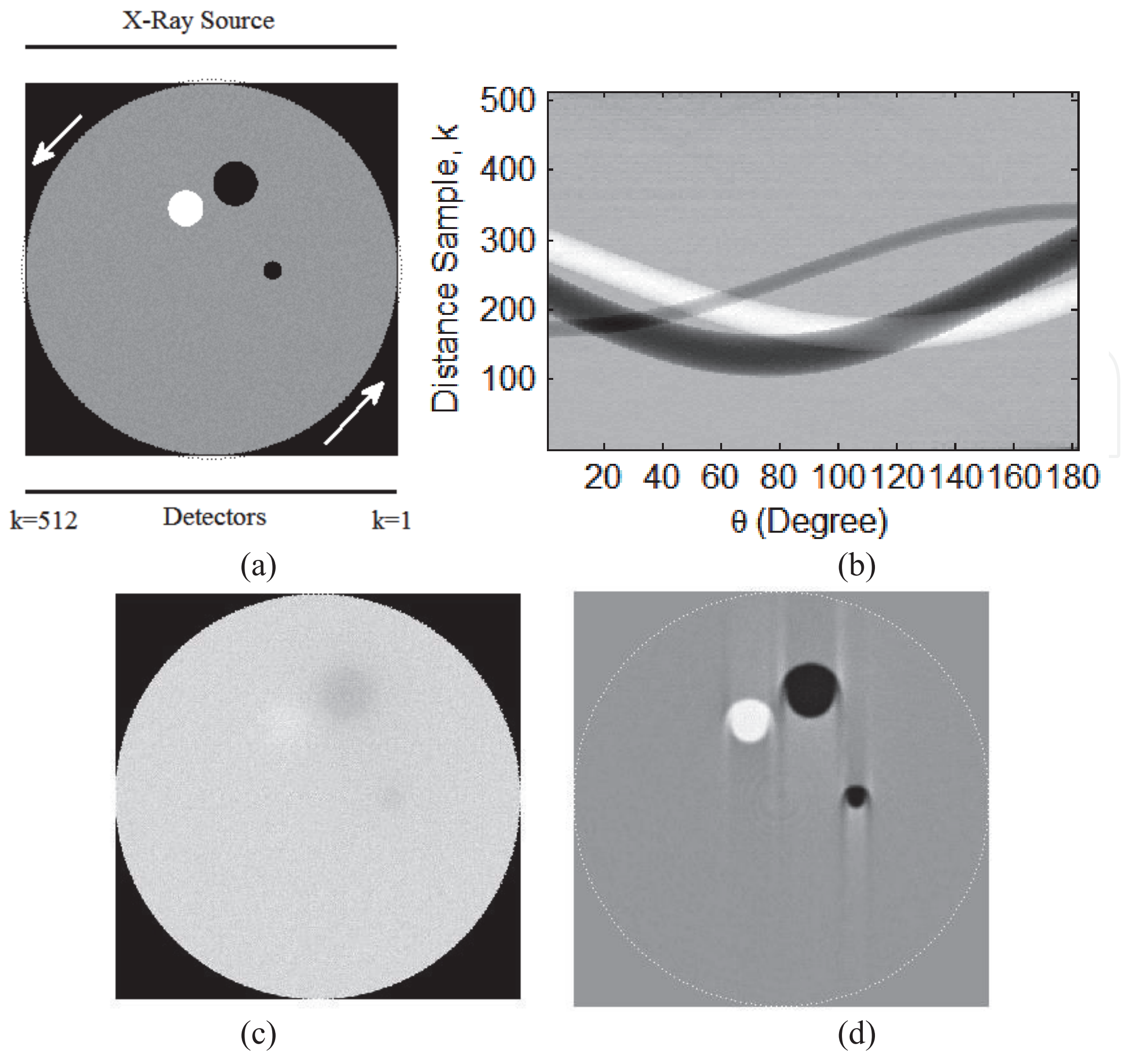


**Figure 8.**
*A backprojection computer simulation example: (a), an intensity function $f(x, y)$ having three objects of different sizes and different absorption coefficients, position of source and detectors are at the start angle $\theta = 0$; (b), sinogram, generated by linear projection in which the distance $s = 2R$, where $R$ is the gantry radius, is sampled into 512 samples, versus $0 \leq \theta \leq \pi$ with step 1 degree; (c), an image generated by backprojection without filtering; and (c) an image generated by filtered backprojection without filtering in which the objects are recovered.*

that we can use 513 detectors uniformly distributed on the maximum width of the scanned target. Thus, each detector receives the intensity projection from the line connecting the detector to an $X$-ray source facing it as shown in the figure. **Figure 8(b)** shows the sinogram due to the linear projection of the intensities versus each of the rotational angle $\theta$ form 0 to 180° with a step of 1°. It is obvious that the sinogram provides information for three objects of different sizes and different absorption coefficients.

### *3.2.2 Fan beam projection*

From **Figure 9**, we can observe that the linear projection on a detector on the arc is parameterized by the detector angle $\alpha$ and the rotational angle $\theta$. Thus, the integration of the intensities of all voxels on the line $\ell(\theta, \alpha)$ is given by

$$g(\theta, \alpha) = \int_{\ell(\theta,\alpha)} f(x, y)dxdy \tag{7}$$

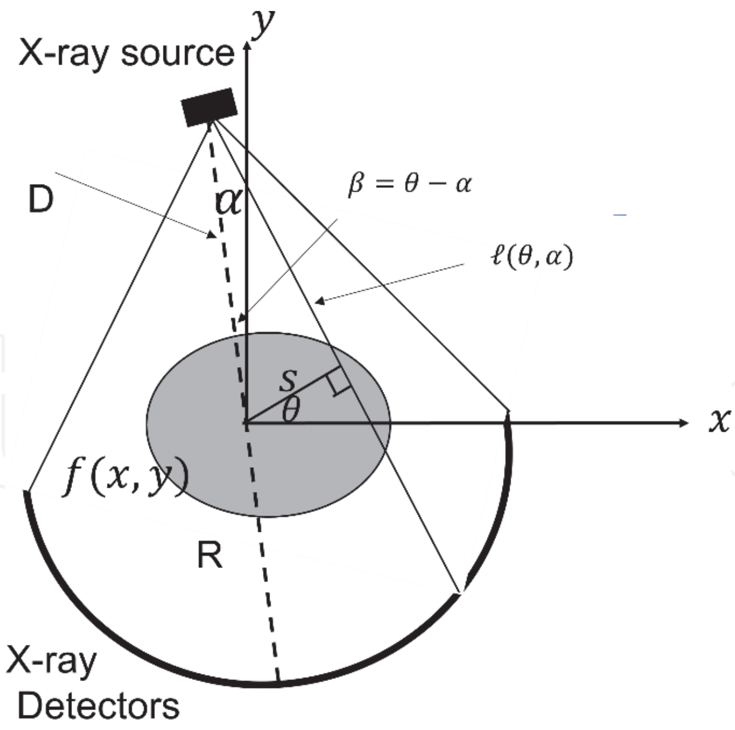


**Figure 9.**
*An intensity function $f(x, y)$ and the fan beam to project this intensity on an array of detectors on the arc defined by the angle $|\alpha| \le \alpha_m$. Both the X-ray source and the detector arc rotate, simultaneously, by the angle $0 \le \theta \le 2\pi$, round the intensity function.*

where

$$\ell(\theta, \alpha) = \{(x, y) : x\cos(\theta) + y\sin(\theta) = D\sin(\alpha)\} \tag{8}$$

**Figure 11(a)** shows a computer simulation scenario for $X$-Ray fan beam. The intensity function is simulated by three objects with different sizes and different absorption coefficients in a background noise. We use 257 detectors uniformly distributed on an arc of 110°, uniformly equiangular, with radius that is equal to the gantry radius, and the $X$-ray source position $D$ is 1.1 of the gantry radius. **Figure 11(b)** shows the sinogram due to the projection versus the rotational angle $\theta$ from 0 to 360° with a step of 1°. It is obvious that the sinogram provides information about three objects of different sizes and different absorption coefficients.

### 3.3 Image reconstruction and backprojection

Backprojection aims at reconstructing an image representing an approximation of the absorption coefficient of each voxel since the true invers is not possible. In linear bean, this backprojection is given by

$$bp(x, y) = \int_0^{\pi} p(\theta, x\cos(\theta) + y\sin(\theta))d\theta \tag{9}$$

However, in fan beam, the projection is given by

$$bg(x, y) = \int_0^{2\pi} g\left(\theta, \sin^{-1}\left(\frac{x\cos(\theta) + y\sin(\theta)}{D}\right)\right)d\theta \tag{10}$$

This implies that in both linear and fan beam projections, each $(x, y)$-voxel accumulates all projected values obtained from all rotational angles, which results in

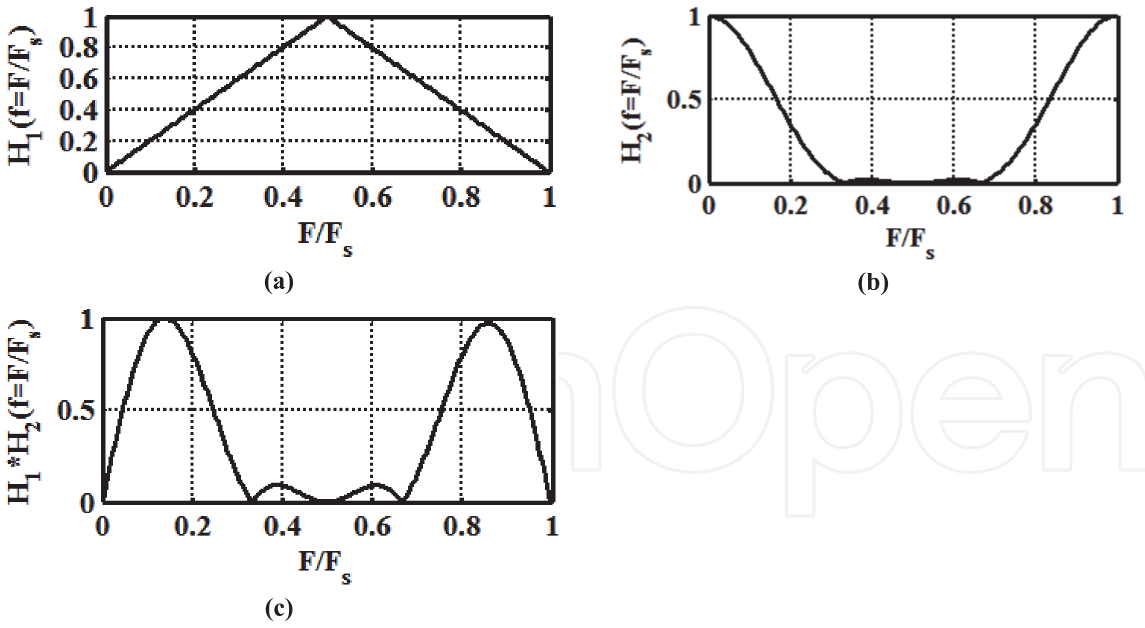


**Figure 10.**
*Frequencies gain of three one-dimensional filters used with backprojection; (a) ramp filter; (b) low-pass filter generated by as a Hanning window; and (c), the multiplication of both filters in the frequency domain normalized to a maximum unity. The filter in (c) is sued for filtering $\boldsymbol{p}(\boldsymbol{\theta}, \boldsymbol{s})$ just before implementing the backprojection algorithm.*

a stare-like blurring image. The voxels of true objects should have sharp intensity edges (positive or negative) compared with its neighborhoods. These sharp edges manifested themself in high frequency; this high frequency increases as the object size decreases. Thus, to remove the blurring and to enhance the resultant backprojection image, a ramp (in frequency domain) filter can be used. In such filter, the gain increases with the increase of the frequency. **Figure 10** shows in (a) the filter's amplitude versus the normalized frequency. It also shows in (b) a lowpass filter designed as a Hanning window. Finally in **Figure 10(c)**, the normalized multiplication of both filters; this resultant bandpass filter is applied to $p(\theta, s)$ just before implementing the backprojection algorithm. The algorithm employs filtering prior to backprojection, called filtered backprojection. **Figures 8(c)** and **11(c)** show the reconstructed images created by the backprojection, without filtering. It is obvious that the images are blurred, and the objects are hidden. However, **Figures 8(d)** and **11(d)** show the images obtained by the filtered backprojection. It is obvious that we get clear image in which simulated objects are manifested.

## 4. Medical applications

### 4.1 Conventional X-ray

Conventional $X$-ray imaging is the prompt and appropriate imaging in Emergency Department patient workup. It can prevent significant morbidity and mortality in all trauma patients. The initial and standard trauma series are $X$-rays of the chest, pelvis, and cervical spine. This should include systematic examination and assessment of alignment, bony structures, cartilage, and soft tissue (ABCS) [58]. In chest diseases, $X$-ray imaging is the first standard technique for pneumonia detection. For both viral and bacterial pneumonia. In COVID-19, conventional $X$-ray plays an important role as a cheap and prompt diagnostic imaging technique.

*DOI: http://dx.doi.org/10.5772/intechopen.101808*

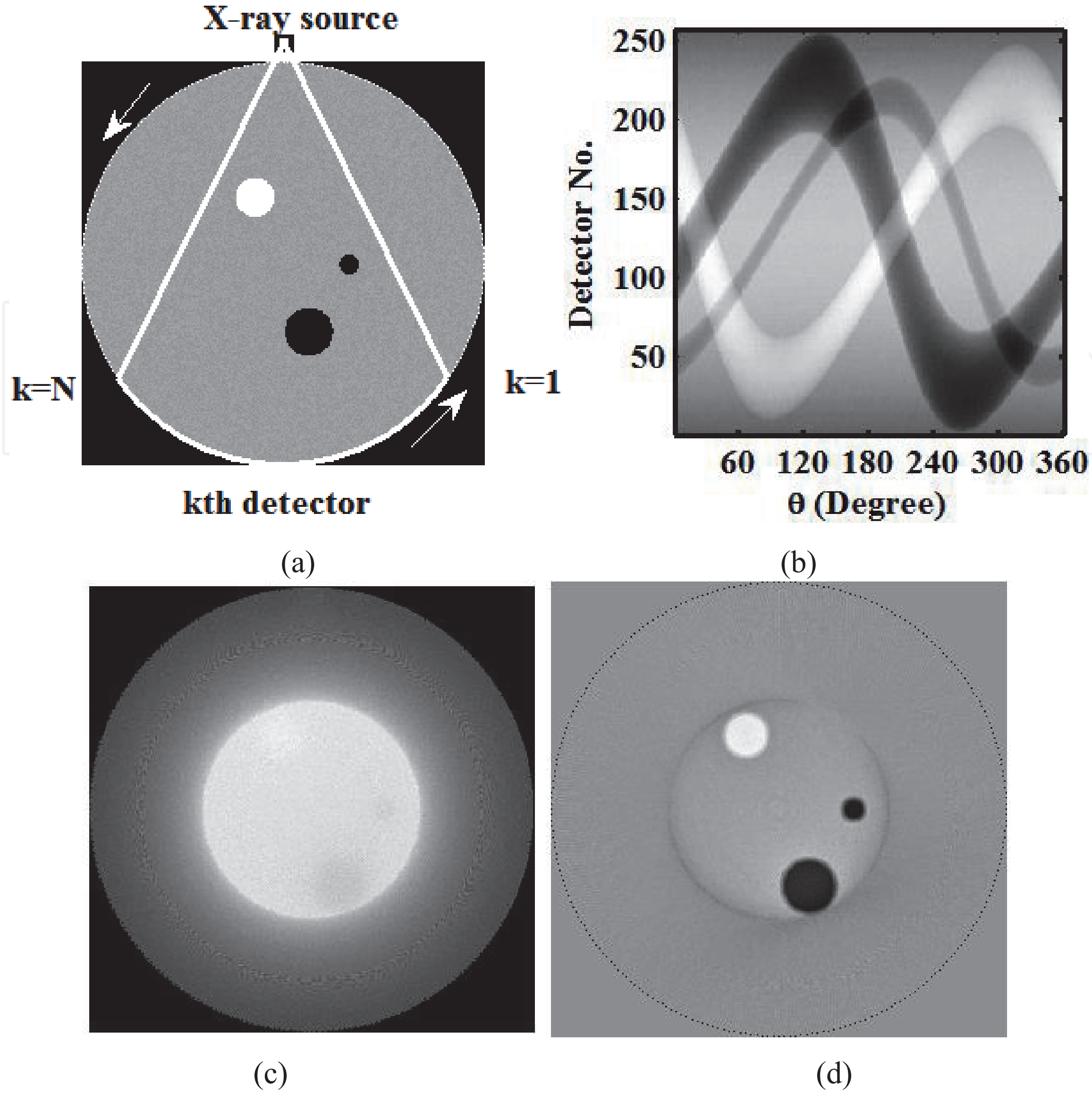


**Figure 11.**
*A backprojection computer simulation example in fan beam- X ray and arc-shaped array of detectors: (a), an intensity function $f(x, y)$ having three objects of different sizes and different absorption coefficients, start position at the start angle $\theta = 0$; (b), sinogram, generated by the arc shape array detector sampled into 257 detectors (equiangular) versus the rotational angle $0 \leq \theta \leq 2\pi$ with a step of 1 degree; (c), an image generated by backprojection without filtering; and (c) an image generated by filtered backprojection in which the objects are recovered.*

**Figures 12** and **13** show the use of *X*-ray imaging of the chest for the diagnosis of bacterial penuomnia and Covid-19.

### 4.2 CT scan

Low radiation load, high resolution, and fast procedure make the CT scan one of the main diagnostic tools and for different health problems. We are just interested in mentioning few CT scan application examples. CT scan could be used for detecting and screening lung carcinoma as shown in **Figure 14**. In COVID-19, CT scan has played an important role for lung instigation COVID-19-induced pneumonia. This pneumonia manifests as itself as bright spots in the image since it absorbs more X-ray energy. **Figure 15** shows in the top row non-COVID CT scan images while in the bottom one shows COVID-19 images. CT scan also is convenient imaging tool for the brain in trauma and normal clinical routine. **Figure 16** shows brain images with hemorrhage in the top row while in the bottom one shows the segmentation for detecting the hemorrhage region. Also, CT scan has been used for the investigation of spinal cord and vertebral column.

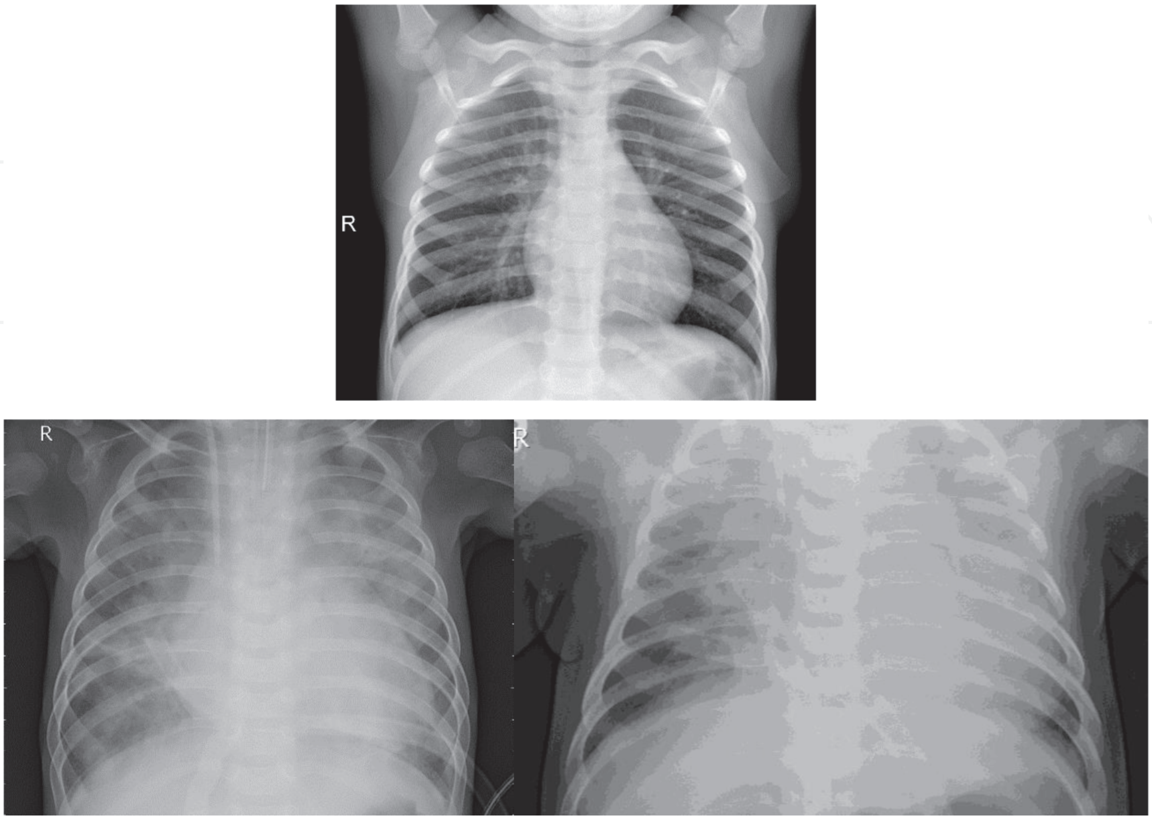


**Figure 12.**
*Chest X-ray image. Top row, normal; bottom row, bacterial pneumonia. From Kaggel.com database: https://www.kaggle.com/tolgadincer/labeled-chest-xray-images.*

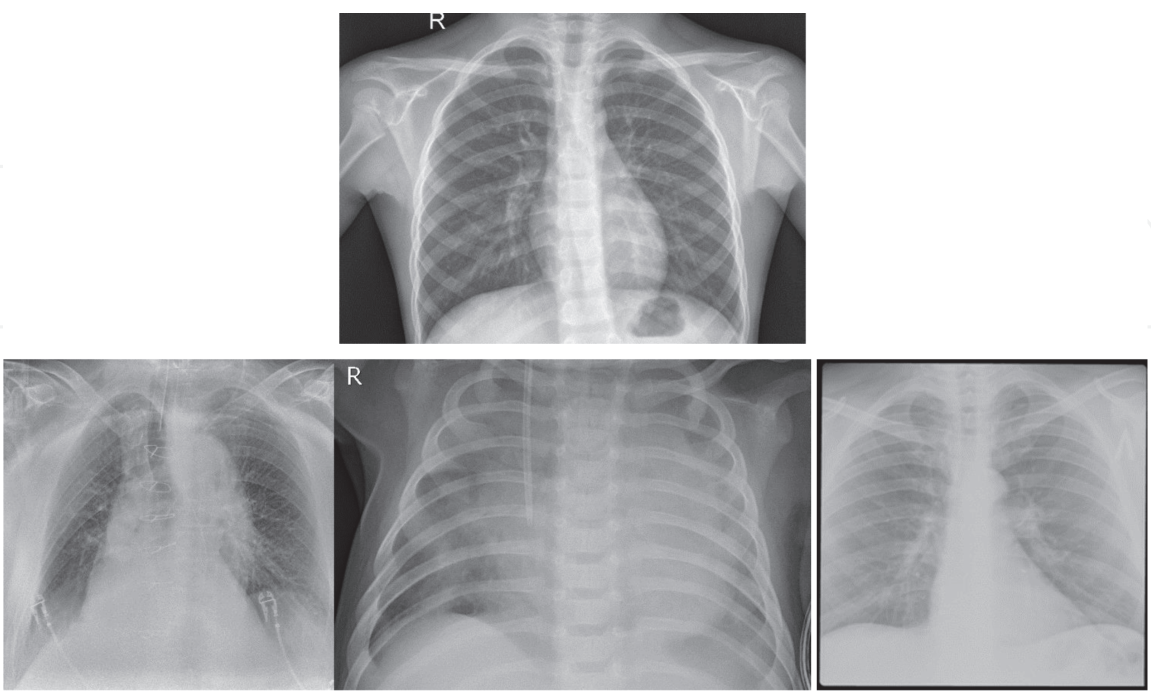


**Figure 13.**
*Chest X-ray image. Top row, normal; bottom row, from left-to-right, COVID-19, bacterial pneumonia, and tuberculosis. From Kaggel.com database: https://www.kaggle.com/jtiptj/chest-xray-pneumoniacovid19tuberc ulosis*

DOI: http://dx.doi.org/10.5772/intechopen.101808

**Figure 14.**
*Chest CT scan slices: Most left, Normal; middle, adenocarcinoma and Most right, carcinoma. From Kaggle.com: https://www.kaggle.com/mohamedhanyyy/chest-ctscan-images.*

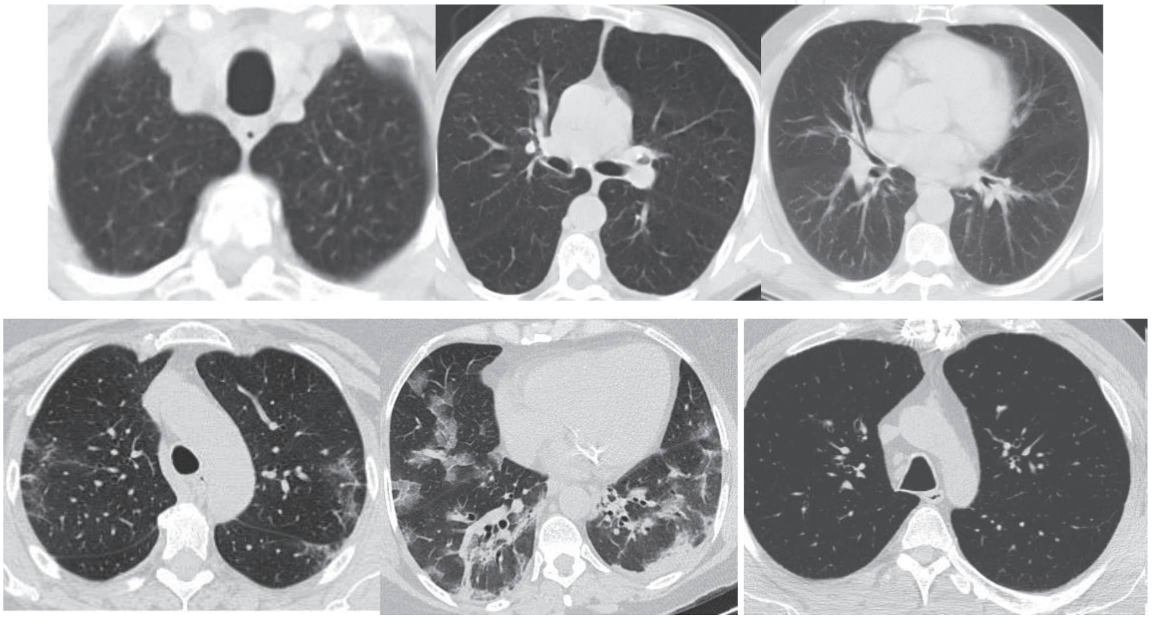

**Figure 15.**
*Chest CT scan slices: Top row, non-COVID, bottom row, COVID. From kaggel.com: https://www.kaggle.com/plameneduardo/sarscov2-ctscan-dataset.*

## 5. Discussion and conclusion

CT scanner has been one of the main diagnostic imaging tools in the medical field. It provides multi two-dimensional slices in the axial plane for abdomen, chest, brain, vertebral column, and spinal cord. It employs low dose of X-ray. It also takes a reasonable time to get CT scan procedure done. More work may be needed to develop CT scan technology affordable for the development countries. Appreciated research efforts are going on to mining and processing the images provided by the CT scanner to develop computer algorithms that can help in improving diagnostic accuracy. These include developing different algorithms in machine learning, image processing, statistical analysis, multi resolution analysis, fast filtered backprojection. Image processing includes noise reduction and image enhancement, features extraction, morphology analysis, image segmentation. Deep learning aims at answering a question of if disease or not disease, e.g., benign tumor or carcinoma one, COVID or non-COVID, based on the given image. In backprojection research, the objective is to develop fast and supper resolution backprojection algorithms and to employ compressive sensing for image reconstruction.

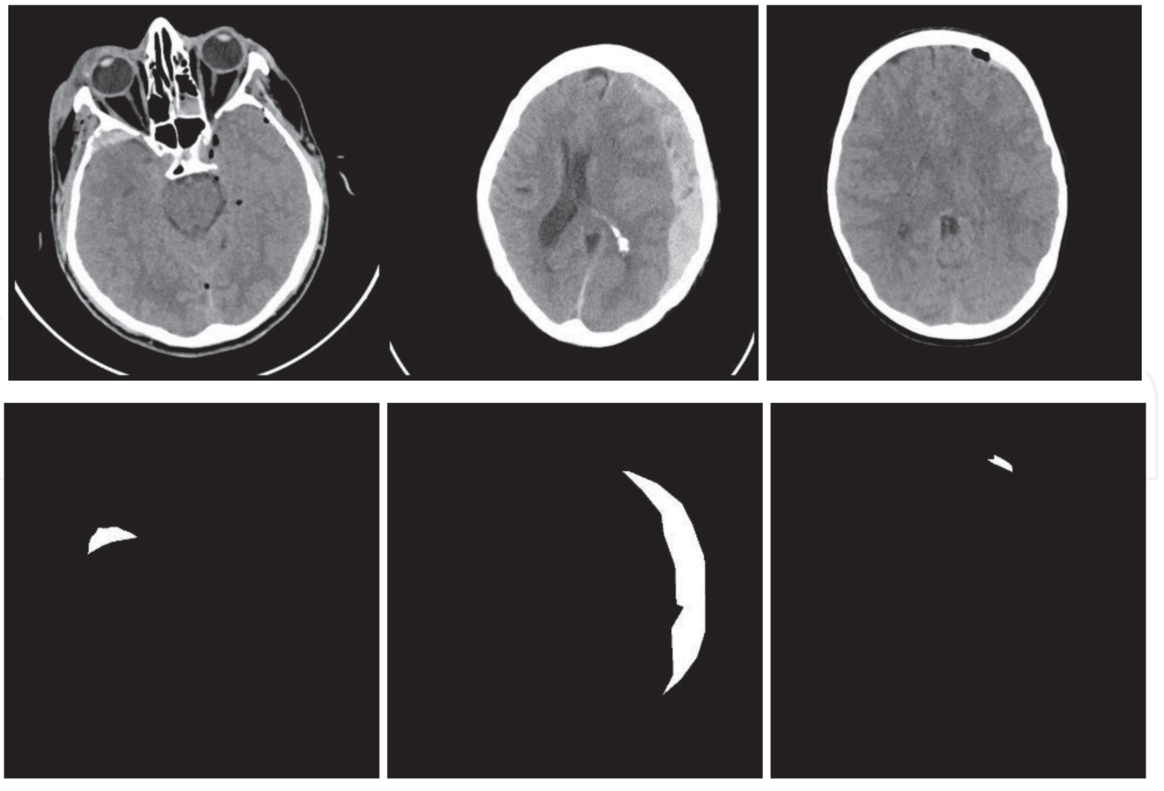

**Figure 16.**
*Brain CT scan: Top row, brain image with intracranial Hemorrhage; bottom row, the segmentation of the image to detect the intracranial Hemorrhage region. From kaggel.com: https://www.kaggle.com/vbookshelf/computed-tomography-ct-images.e*

## Conflict of interest

The author declares no conflict of interest.




## Author details

Reda R. Gharieb
Assiut University, Egypt

*Address all correspondence to: rrgharieb@gmail.com

## References

[1] Friel JJ, Lyman CE. Tutorial review: X-ray mapping in electron-beam instruments. Microscopy and Microanalysis. 2006;**12**(1):2-25

[2] Nascimento MLF. Brief history of X-ray tube patents. World Patent Information. 2014;**37**:48-53

[3] Wagner JP, Chung KC. A historical report on Robert Kienböck (1871–1953) and Kienböck's disease. The Journal of Hand Surgery. 2005;**30**(6):1117-1121

[4] Linton OW. Medical applications of x rays. Beam Line. 1995;**25**(2):25-34

[5] Pasveer B. Knowledge of shadows: The introduction of X-ray images in medicine. Sociology of Health & Illness. 1989;**11**(4):360-381

[6] Mould RF. The early history of x-ray diagnosis with emphasis on the contributions of physics 1895-1915. Physics in Medicine & Biology. 1995; **40**(11):1741

[7] Yaffe MJ, Rowlands JA. X-ray detectors for digital radiography. Physics in Medicine & Biology. 1997; **42**(1):1-39

[8] Gruner SM, Tate MW, Eikenberry EF. Charge-coupled device area X-ray detectors. Review of Scientific Instruments. 2002;**73**(8): 2815-2842

[9] Bertuccio G, Caccia S, Puglisi D, Macera D. Advances in silicon carbide X-ray detectors. Nuclear Instruments and Methods in Physics Research Section A: Accelerators, Spectrometers, Detectors and Associated Equipment. 2011;**652**(1):193-196

[10] Spahn M. X-ray detectors in medical imaging. Nuclear Instruments and Methods in Physics Research Section A: Accelerators, Spectrometers, Detectors and Associated Equipment. 2013;**731**: 57-63

[11] Dong Y, Pan Y, Zhang J, Xu W. Learning to read chest X-ray images from 16000+ examples using CNN. In: 2017 IEEE/ACM International Conference on Connected Health: Applications, Systems and Engineering Technologies (CHASE). Philadelphia, Pennsylvania, USA: IEEE; 2017. pp. 51-57

[12] Parveen N, Mohamed Sathik M. Detection of pneumonia in chest X-ray images. Journal of X-Ray Science and Technology. 2011;**19**(4):423-428

[13] Zhang J, Xie Y, Pang G, Liao Z, Verjans J, Li W, et al. Viral pneumonia screening on chest X-rays using confidence-aware anomaly detection. IEEE Transactions on Medical Imaging. 2021;**40**(3):879-890

[14] Ausawalaithong W, Thirach A, Marukatat S, Wilaiprasitporn T. Automatic lung cancer prediction from chest X-ray images using the deep learning approach. In: 2018 11th Biomedical Engineering International Conference (BMEICON). Thailand: IEEE; 2018. pp. 1-5

[15] Becker AS, Blüthgen C, Sekaggya-Wiltshire C, Castelnuovo B, Kambugu A, Fehr J, et al. Detection of tuberculosis patterns in digital photographs of chest X-ray images using Deep Learning: Feasibility study. The International Journal of Tuberculosis and Lung Disease. 2018;**22**(3):328-335

[16] Imran A-A-Z, Terzopoulos D. Semi-supervised multi-task learning with chest X-ray images. In: International Workshop on Machine Learning in Medical Imaging. Cham: Springer; 2019. pp. 151-159

[17] Rahman T, Khandakar A, Abdul Kadir M, Rejaul Islam K, Islam KF,

Mazhar R, et al. Reliable tuberculosis detection using chest X-ray with deep learning, segmentation and visualization. IEEE Access. 2020;**8**: 191586-191601

[18] Chandra TB, Verma K, Singh BK, Jain D, Netam SS. Automatic detection of tuberculosis related abnormalities in chest X-ray images using hierarchical feature extraction scheme. Expert Systems with Applications. 2020;**158**:113514

[19] Wu H, Xie P, Zhang H, Li D, Cheng M. Predict pneumonia with chest X-ray images based on convolutional deep neural learning networks. Journal of Intelligent & Fuzzy Systems. 2020; **39**(3):2893-2907

[20] Matsumoto T, Kodera S, Shinohara H, Ieki H. Yamaguchi T, Higashikuni Y, Kiyosue A, et al. Diagnosing heart failure from chest X-ray images using deep learning. International Heart Journal. 2020;**61**(4): 781-786

[21] Dallal AH, Agarwal C, Arbabshirani MR, Patel A, Moore G. Automatic estimation of heart boundaries and cardiothoracic ratio from chest x-ray images. In: Medical Imaging: Computer-Aided Diagnosis. Vol. 10134. USA: International Society for Optics and Photonics; 2017. p. 101340K

[22] Arndt H, Busse A, Meinel FG. Heart and lung in X-ray images: Lost art (?). Radiologe. 2020;**60**(12):1122-1130

[23] Hascoët S, Warin-Fresse K, Baruteau A-E, Hadeed K, Karsenty C, Petit J, et al. Cardiac imaging of congenital heart diseases during interventional procedures continues to evolve pros and cons of the main techniques. Archives of Cardiovascular Diseases. 2016;**109**(2):128-142

[24] Lu L, Sun RR, Liu M, Zheng Y, Zhang P. The inflammatory heart diseases: Causes, symptoms, and treatments. Cell Biochemistry and Biophysics. 2015;**72**(3):851-855

[25] Modlesky CM, Bickel CS, Slade J, Dudley GA. Assessment of skeletal muscle mass in men with spinal cord injury using dual energy X-ray absorptiometry and magnetic resonance imaging. Journal of Applied Physiology. 2004;**96**(2):561-566

[26] Parizel PM, Zijden T, Gaudino S, Spaepen M, Voormolen MHJ, Venstermans C, et al. Trauma of the spine and spinal cord: Imaging strategies. European Spine Journal. 2010;**1**(19):8-17

[27] Edwards WB, Schnitzer TJ. Bone imaging and fracture risk after spinal cord injury. Current Osteoporosis Reports. 2015;**13**(5):310-317

[28] Pearcy MJ, Whittle MW. Movements of the lumbar spine measured by three-dimensional X-ray analysis. Journal of Biomedical Engineering. 1982;**4**(2):107-112

[29] McVey G, Sandborg M, Dance DR, Carlsson GA. A study and optimization of lumbar spine X-ray imaging systems. The British Journal of Radiology. 2003; **76**(903):177-188

[30] Antani S, Rodney Long L, Thoma GR, Lee DJ. Anatomical shape representation in spine x-ray images. In: Proceedings of IASTED International Conference on Visualization, Imaging and Image Processing. 2003. pp. 510-515

[31] Jingqi JRTG. Progress of radiological research on digestive system malignancy related sarcopenia. Interventional Journal of Medical Radiology. 2020;**43**(4):457

[32] Pisano ED, Yaffe MJ. Digital mammography. Radiology. 2005; **234**(2):353-362

[33] Mazess RB, Barden HS, Bisek JP, Hanson J. Dual-energy x-ray absorptiometry for total-body and regional bone-mineral and soft-tissue composition. The American Journal of Clinical Nutrition. 1990;**51**(6):1106-1112

[34] Pietrobelli A, Formica C, Wang Z, Heymsfield SB. Dual-energy X-ray absorptiometry body composition model: Review of physical concepts. American Journal of Physiology-Endocrinology And Metabolism. 1996; **271**(6):E941-E951

[35] Hounsfield GN. Computerized transverse axial scanning (tomography): Part 1. Description of system. The British Journal of Radiology. 1973; **46**(552):1016-1022

[36] Chabat F, Yang G-Z, Hansell DM. Obstructive lung diseases: Texture classification for differentiation at CT. Radiology. 2003;**228**(3):871-877

[37] Bonelli FS, Hartman TE, Swensen SJ, Sherrick A. Accuracy of high-resolution CT in diagnosing lung diseases. AJR. American Journal of Roentgenology. 1998;**170**(6):1507-1512

[38] Johkoh T, Müller NL, Akira M, Ichikado K, Suga M, Ando M, et al. Eosinophilic lung diseases: Diagnostic accuracy of thin-section CT in 111 patients. Radiology. 2000;**216**(3): 773-780

[39] Raoof S, Raoof S, Naidich D. Imaging of unusual diffuse lung diseases. Current Opinion in Pulmonary Medicine. 2004;**10**(5):383-389

[40] Makaju S, Prasad PWC, Alsadoon A, Singh AK, Elchouemi A. Lung cancer detection using CT scan images. Procedia Computer Science. 2018;**125**:107-114

[41] Gong T, Liu R, Lim Tan C, Farzad N, Kiang Lee C, Chuan Pang B, et al. Classification of CT brain images of head trauma. In: IAPR International Workshop on Pattern Recognition in Bioinformatics. Berlin, Heidelberg: Springer; 2007. pp. 401-408

[42] Shahangian B, Pourghassem H. Automatic brain hemorrhage segmentation and classification in CT scan images. In: 2013 8th Iranian Conference on Machine Vision and Image Processing (MVIP). IEEE; 2013. pp. 467-471

[43] Yahiaoui AFZ, Bessaid A. Segmentation of ischemic stroke area from CT brain images. In: 2016 International Symposium on Signal, Image, Video and Communications (ISIVC). IEEE; 2016. pp. 13-17

[44] Wijdicks EFM. The first CT scan of the brain: entering the neurologic information age. Neurocritical Care. 2018;**28**(3):273-275

[45] Rabinstein AA. Traumatic spinal cord injury. In: Rabinstein A, editor. Neurological Emergencies: A Practical Approach. Cham: Springer; 2020. pp. 271-280

[46] Barba CA, Taggert J, Morgan AS, Guerra J, Bernstein B, Lorenzo M, et al. A new cervical spine clearance protocol using computed tomography. Journal of Trauma and Acute Care Surgery. 2001; **51**(4):652-657

[47] Gupta PK, Krishna A, Dwivedi AN, Gupta K, Madhu B, Gouri G, et al. CT scan findings and outcomes of head injury patients: A cross sectional study. Journal of Pioneering Medical Sciences. 2011;**1**(3):78-82

[48] Kligman M, Vasili C, Roffman M. The role of computed tomography in cervical spinal injury due to diving. Archives of Orthopedic and Trauma Surgery. 2001;**121**(3):139-141

[49] Zeng GL. Image reconstruction: A tutorial. Computerized Medical Imaging and Graphics. 2001;**25**(2):97-103

[50] Hanson KM. On the optimality of the filtered backprojection algorithm. Journal of Computer Assisted Tomography. 1980;**4**(3):361-363

[51] Li J, Jaszczak RJ, Wang H, Coleman RE. A filtered-backprojection algorithm for fan-beam SPECT which corrects for patient motion. Physics in Medicine & Biology. 1995;**40**(2): 283-294

[52] Hiriyannaiah HP. X-ray computed tomography for medical imaging. IEEE Signal Processing Magazine. 1997;**14**(2): 42-59

[53] Wei Y, Wang G, Hsieh J. Relation between the filtered backprojection algorithm and the backprojection algorithm in CT. IEEE Signal Processing Letters. 2005;**12**(9):633-636

[54] Beister M, Kolditz D, Kalender WA. Iterative reconstruction methods in X-ray CT. Physica Medica. 2012;**28**(2): 94-108

[55] Seibert JA, Boone JM. X-ray imaging physics for nuclear medicine technologists. Part 2: X-ray interactions and image formation. Journal of Nuclear Medicine Technology. 2005;**33**(1):3-18

[56] Stanford RW, Hills TH. An advance in X-ray film processing. The British Journal of Radiology. 1956;**29**(341): 286-294

[57] Hoheisel M. Review of medical imaging with emphasis on X-ray detectors. Nuclear Instruments and Methods in Physics Research, Section A: Accelerators, Spectrometers, Detectors and Associated Equipment. 2006; **563**(1):215-224

[58] Gay DAT, Miles R. Use of imaging in trauma decision-making. BMJ Military Health. 2011;**157**(Suppl 3): S289-S292